Catalysis Science & Technology

ROYAL SOCIETY OF CHEMISTRY

PAPER

View Article Online
View Journal | View Issue

Cite this: *Catal. Sci. Technol.*, 2020, 10, 690

A facile acid treatment for P25 modification with enhanced photocatalytic H_2 evolution – effect of Brønsted acid sites and oxygen vacancies†

Chao Lv, Xuefang Lan, Fuqiang Li, Lili Wang, Liqi Xiao, Cheng Wang, Jinsheng Shi and Shuguang Yu *

Received 28th October 2019,
Accepted 14th December 2019

DOI: 10.1039/c9cy02166c

rsc.li/catalysis

Acid treated P25 catalysts (HP25-*x*, *x* represents the treatment temperature) were successfully fabricated *via* a simple soaking and drying process for photocatalytic H_2 production. After acid treatment, a substantial number of –OH groups were obtained on the surface of HP25-60, which can act as Brønsted acid sites providing hydrogen protons for H_2 generation. Besides, more oxygen vacancies and Ti^{3+} sites were also created on the HP25-60 surface after acid treatment, which could enhance the carrier separation and transfer efficiency by capturing more electrons and holes, respectively. The H_2 production over HP25-60 reached 4853 μmol h^{-1} with Pt as a co-catalyst, which is 7.1 times higher than 679 μmol h^{-1} of bare TiO_2. Three favorable factors for H_2 photogeneration, *i.e.* Brønsted acid sites, oxygen vacancies and Ti^{3+} sites, can be introduced on a catalyst surface *via* a simple one-step acid strategy, which can be applied as a universally-applicable modification method for valence-alternative metal oxide semiconductors for enhanced H_2 photogeneration.

1. Introduction

Motivated by the increasing demand for a renewable and clean energy source in the future, hydrogen production from water-splitting by solar energy has been the subject of extensive investigations.[1–7] Semiconductor photocatalysts are the key part for H_2 photogeneration,[1,4,8] and among multifarious semiconductors, TiO_2 has been proven to be the most suitable candidate for H_2 photogeneration as a result of its high chemical stability, low cost, and strong oxidizing and reducing ability.[1] Unfortunately, the photocatalytic H_2-production efficiency on bare TiO_2 is very low due to the rapid carrier recombination and the large H_2 production overpotential.[2,9] To address these limitations, a number of efforts have been made, including noble-metal deposition,[10] semiconductor composition,[11] dye sensitization,[12] ion doping,[13] *etc.*

Besides the modification strategies mentioned above, acid treatment of TiO_2 is another simple and effective modification approach to improve the photocatalytic activity of TiO_2. Se-Keun Park and Hyunho Shin[14] have explored the effect of HCl and H_2SO_4 treatment on TiO_2 powder and its performance in the degradation of rhodamine B. They found that the acid treatment could enhance RhB adsorption on the TiO_2 surface by protonation of the –COOH group *via* the Brønsted acid sites introduced by acid treatment. Sancun Hao[15] and Kyung-Hee Park[16] *et al.* reported that acid-treated TiO_2 could improve the photovoltaic properties of dye-sensitized solar cells by increasing the dye absorption and decreasing the charge-transfer resistance. Although acid-treated TiO_2 has been applied in the domain of dye degradation and dye-sensitized solar cells, the application of acid-treated TiO_2 in photocatalytic H_2 production has never been investigated.

Herein, we applied an acid-treated P25 catalyst in H_2 photogeneration, expecting that the Brønsted acid site introduced by acid treatment could enhance the H_2 production by providing more protons. Moreover, plenty of oxygen vacancies and Ti^{3+} sites can be introduced in P25 by acid treatment, which could capture electrons contributing to a higher carrier separation efficiency and hence a higher H_2 evolution rate during photoreaction. Such a simple strategy for enhanced photogeneration of H_2 has never been reported before.

2. Experimental

2.1 Synthesis of HP25-60

HP25-*x* catalysts were prepared by acid treatment as follows: typically, 5 g P25 (≥99.8%, Sigma Aldrich) was immersed in 6 M hydrochloric acid (HCl, 36–38%, Sigma Aldrich) for 5

Department of Chemistry and Pharmaceutical Science, Qingdao Agricultural University, Chengyang District, Qingdao, China. E-mail: jsshiqn@aliyun.com

† Electronic supplementary information (ESI) available. See DOI: 10.1039/c9cy02166c

hours. Then the acid treated P25 was dried at 60 °C for 6 h and then heated at 60, 100, 200, and 300 °C for 3 h in an air atmosphere with a heating rate of 3 °C min^{-1}. The samples obtained at different treatment temperatures are labeled as HP25-*x*, where *x* refers to the treatment temperature (*x* = 60, 100, 200 and 300 °C).

2.2 Characterization

The crystal structure of the samples was observed using an X-ray diffractometer (XRD; Bruker D8 Advance X-ray diffractometer) at 40 kV and 40 mA equipped with a Cu anode X-ray tube (Cu Kα X-rays, λ = 1.54056 Å). The morphology of the 3DOM Sr–TiO_2 sample was observed by scanning electron microscopy (SEM, Hitachi S-4800) and transmission electron microscopy (TEM, TALOS F200). The adsorption–desorption isotherms and the pore size distributions of the catalysts were examined using volumetric adsorption equipment (NOVA Surface Area Analyzer Station A, USA). Ultraviolet visible (UV-vis) diffuse reflectance spectroscopy (DRS) was performed using a UV-vis spectrophotometer (TU-1901, China) in the range of 200–800 nm with $BaSO_4$ as the reference. The photoluminescence (PL) spectra were recorded using a Hitachi fluorescence spectrophotometer (F-7000) and the excitation wavelength was set at 264 nm.

2.3 Photoelectrochemical measurements

Photoelectrochemical measurements were conducted with an Autolab PGSTAT302 N assembled with a 300 W Xe lamp in the frequency range of 10–100 kHz in a standard three-electrode system using fabricated photocatalyst films as working electrodes, a Pt plate electrode as the counter electrode and an Hg/Hg_2Cl_2 (saturated in KCl) electrode as the reference electrode. The transient photocurrent response was measured in 0.5 mol L^{-1} Na_2SO_4 electrolyte with light on/off cycles for different samples under visible light irradiation at a bias of 0 V *vs.* Hg/Hg_2Cl_2. To prepare the working electrode, the photocatalyst (4 mg) and 5 wt% Nafion solution (80 μL) were dispersed in isopropyl alcohol (920 μL) and sonicated for at least 1 h to form a homogeneous mixture. Then, the mixture (40 μL) was dropped cast on a 5 cm × 1 cm fluorine-doped tin oxide (FTO) glass electrode. Electrochemical impedance spectroscopy (EIS) tests were conducted in the same configuration at η = −0.6 V (*vs.* RHE) from 10^5–10^{-1} Hz with an AC voltage of 20 mV. Mott–Schottky (M–S) plots were obtained at a frequency of 1000 Hz.

2.4 Photocatalytic water splitting

The photocatalytic hydrogen evolution activities of different samples were tested by using a photocatalytic activity evaluation system (Labsolar-6A, Perfectlight, Beijing). Typically, 30 mg catalyst was added into an aqueous solution (90 mL) of triethanolamine (TEOA, 10 vol%, as a sacrificial reagent). 238 μL H_2PtCl_6 solution (3 wt% Pt) was added into the above mixture, which was then exposed to light for 0.5 h to load Pt nanoparticles on the samples. Before irradiation, the whole system was sealed and vacuumed using a mechanical pump to eliminate any gas impurities. Then, the produced hydrogen was extracted every 1 hour with an online gas chromatograph (GC7900, Techcomp, Shanghai) equipped with a TCD and N_2 carrier. A 300 W Xe lamp without any filters was used as the light source. The generated amount of hydrogen was evaluated according to the fitted standard curve. The apparent quantum yield (AQY) was calculated based on eqn (1). The light intensity was *ca.* 105.26 mW cm^{-2} and the illuminated area for the reactor was about 28 cm^2.

$$\mathrm{AQY}(\%) = \frac{\text{number of reacted electrons}}{\text{number of incident photons}} \times 100\% = \frac{\text{number of evolved } H_2 \text{ molecules}}{\text{number of incident photons}} \quad (1)$$

3. Results and discussion

3.1 Solid characterization

XRD was applied to detect the crystalline phases of P25 and HP25-*x* (Fig. 1). The sharp diffraction peaks at 2θ = 25.3°, 36.9°, 37.8°, 38.6°, 48.0° and 53.9° are assigned to the (101), (103), (004), (112), (200) and (105) planes of anatase phase TiO_2 (JCPDS, No. 21-1272), respectively.[17] And the sharp diffraction peaks at 2θ = 27.5°, 36.1°, 39.2°, 41.3°, 44.1° and 56.7° are ascribed to the (110), (101), (200), (111), (210) and (220) planes of rutile phase TiO_2 (JCPDS, No. 21-1276), respectively.[18] Both the anatase and rutile phases are observed on untreated P25. In comparison to untreated P25, the diffraction of acid treated P25 shows no appreciable changes, indicating that the acid treatment does not destroy the crystal structure of P25. The XRD peaks decrease as the heating temperature increases. This suggests that the crystallinity of HP25-*x* decreases with the increase of treatment temperature.

To view the morphology of P25 and HP25-*x* (*x* = 60, 100), SEM images were obtained (Fig. 2). Before the acid treatment,

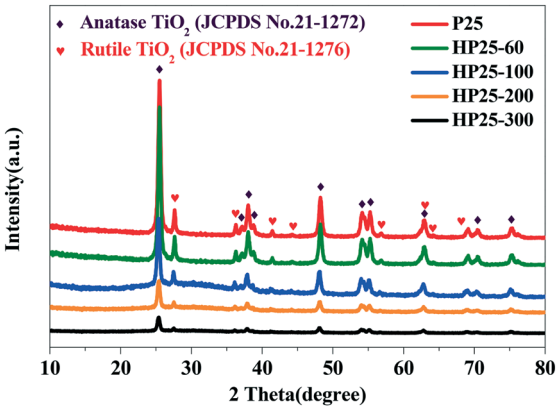

Fig. 1 XRD patterns of P25 and HP25-*x* (*x* = 60, 100, 200 and 300).

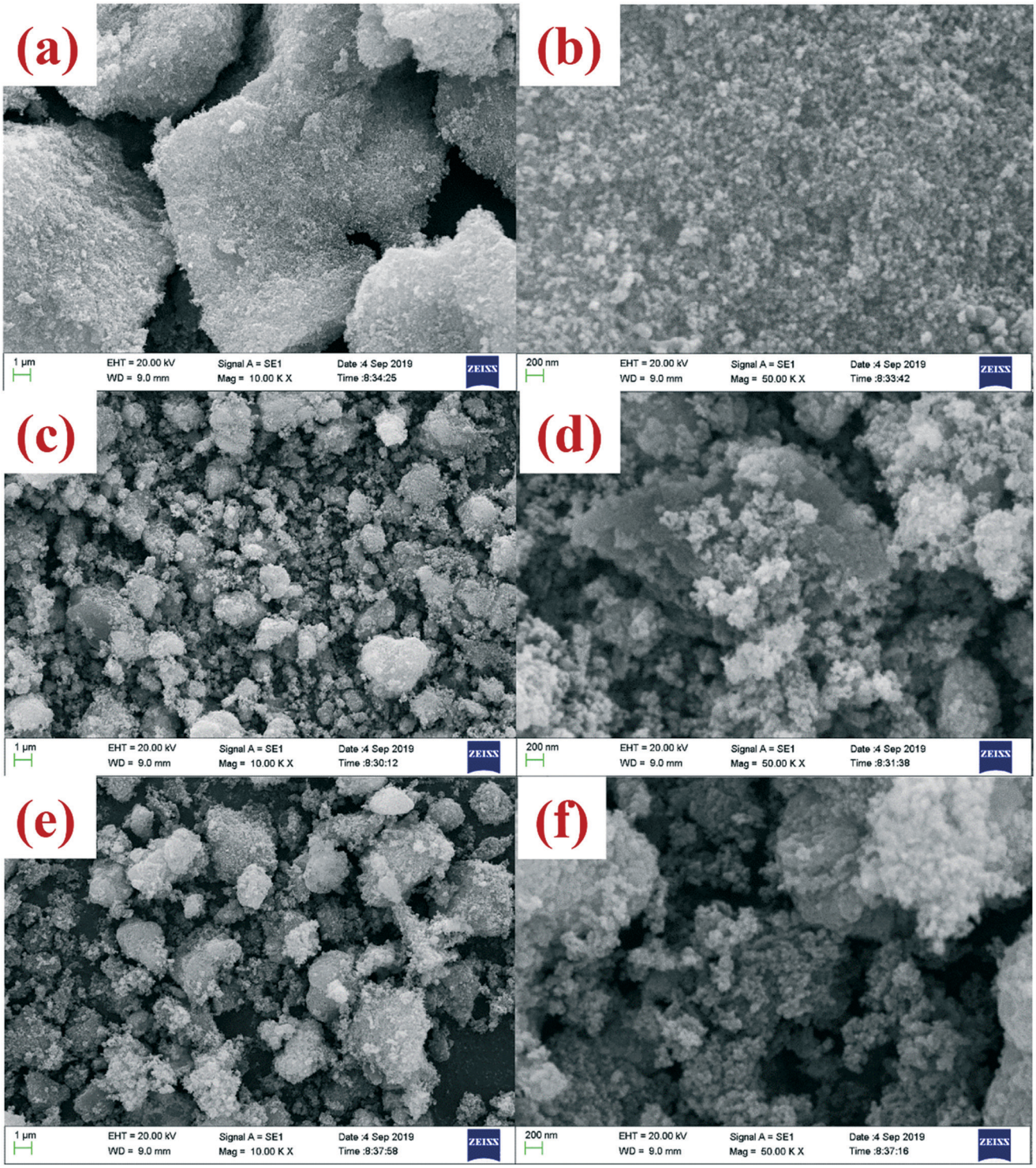

Fig. 2 SEM images of acid-treated P25 (a and b), HP25-60 (c and d) and HP25-100 (e and f).

many large particles of tens of microns were observed in the image of P25. After acid treatment, these large particles were etched into small irregular particles ranging from less than 1 μm to 3 μm. Because the morphologies of HP25-60 and HP25-100 are similar in SEM (Fig. 2), TEM was further carried out to obtain a more micro view of these samples (Fig. 3). The results show that HP25-60 and HP25-100 still possess similar morphologies with small particles about 20–30 nm observed under high resolution TEM.

XPS measurements were also performed to elucidate the chemical valence state and the surface component of P25 and HP25-*x* (Fig. 4). The peaks located at 458.6 and 457.6 eV are assigned to Ti^{4+} $2p_{3/2}$ and Ti^{3+} $2p_{3/2}$, respectively.[19] The Ti^{3+} content in P25 is substantially increased after acid

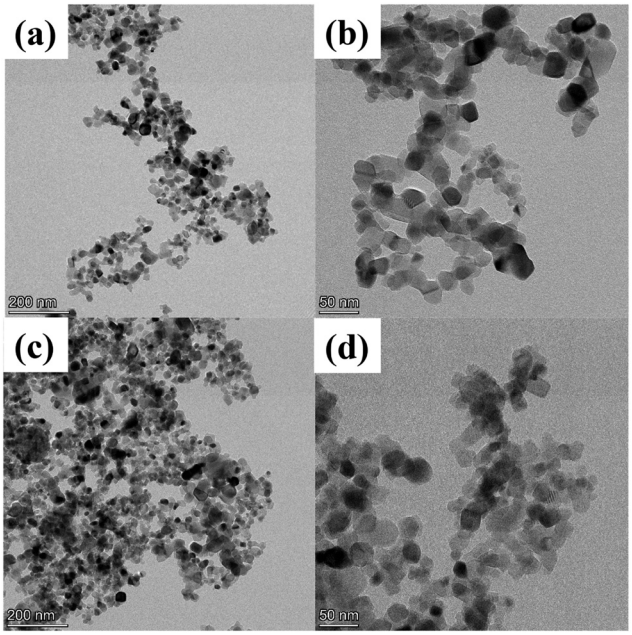

Fig. 3 TEM images of (a and b) P25-60 and (c and d) HP25-100.

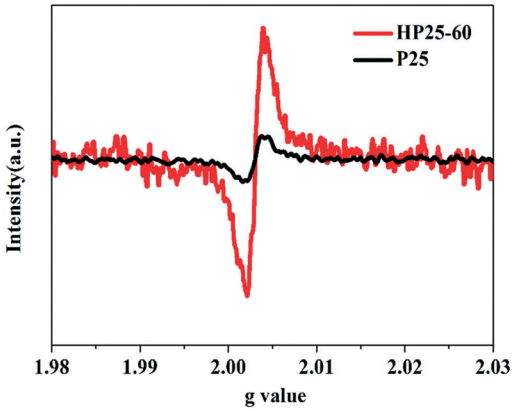

Fig. 5 ESR spectra of O_v over P25 and HP25-60.

treatment at 60 °C, which is consistent with previous reports[16] and is expected to broaden the light absorption scope by introducing an impurity level.[19] Once the treatment temperature increases to 100 °C, the Ti^{3+} content decreases likely because the heating process in air favors the re-oxidation of Ti^{3+} with O_2.

The O peaks at 529.5 eV, 530.3 eV and 531.9 eV are ascribed to the O lattice (Ti^{4+}–O), the O-atoms in the vicinity of oxygen vacancies (O_v, *i.e.* Ti^{3+}–O) and the –OH bonds,[19] respectively. The O_v content first increases after acid treatment at 60 °C, then decreases after treatment at 100 °C. The variation trend of O_v content on the catalyst surface is consistent with that of Ti^{3+}, which is quite reasonable since the O_v formation is accompanied with the presence of Ti^{3+}. Notably, the –OH groups are also substantially increased on the TiO_2 surface after acid treatment at 60 °C because TiO_2 tends to be protonated at acidic pH levels.[20,21] Once the treatment temperature increases to 100 °C, the –OH groups significantly decrease due to the dehydroxylation effect at high temperature.

The existence of O_v was further verified by ESR. In contrast to P25 that shows a small ESR peak, HP25-60 exhibits much steeper peaks at g = 2.003 (Fig. 5), which are assigned to electrons trapped by oxygen vacancies.[22–25] These results suggest that a large number of oxygen vacancies are generated on the surface of the acid-treated catalyst, consistent with the O_v information obtained by XPS.

The FT-IR spectra of P25 and HP25-x (x = 60 and 100) samples are also obtained to characterize the surface –OH groups on P25 before and after acid treatment (Fig. 6). The bands at 3420 cm^{-1} and 1632 cm^{-1} are assigned to the stretching vibrations and the bending vibrations of adsorbed water, respectively.[14,26] The bands at 3640 cm^{-1} and 1260–

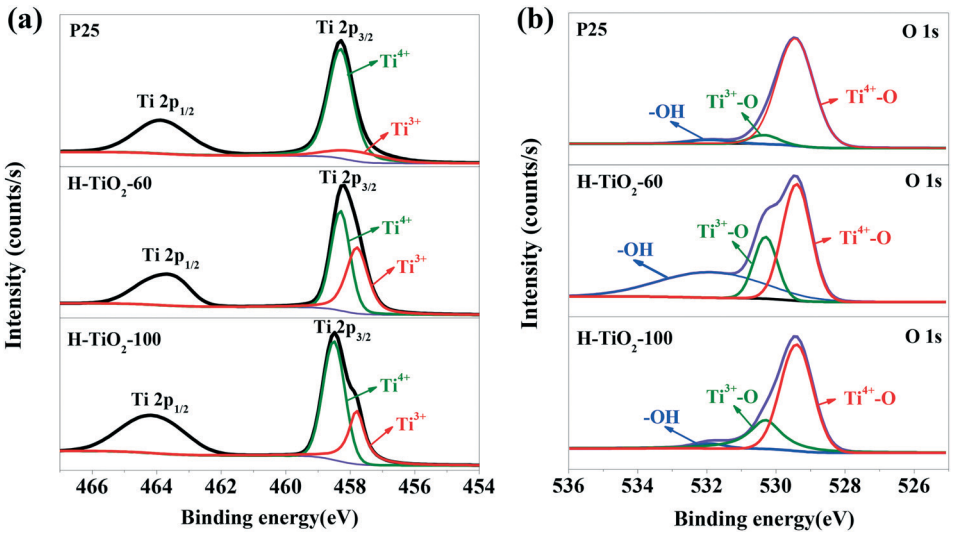

Fig. 4 XPS spectra of (a) the Ti 2p region and (b) the O 1s region for P25 and HP25-x (x = 60 and 100).

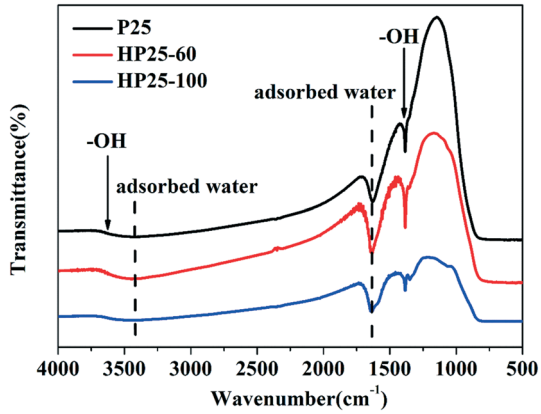

Fig. 6 FT-IR spectra of P25 and HP25-*x* (*x* = 60 and 100).

1350 cm^{-1} are assigned to the stretching vibrations and the bending vibrations of –OH groups, respectively.[27–29] Notably, the amount of adsorbed water and –OH groups both increased substantially on the P25 surface after acid treatment at 60 °C. Once the treatment temperature further increased to 100 °C, the amount of adsorbed water and –OH groups both decreased significantly. These results are consistent with the information obtained from the XPS spectra of the O 1s region.

3.2 Specific surface area analysis

The N_2 adsorption–desorption isotherms of these samples are shown in Fig. 7 and Table 1. All the samples present a type IV isotherm with a typical H_3 hysteresis loop, indicating the existence of a pore structure.[17] After acid treatment, the surface area and pore volume were substantially increased due to the etching effect of acid on TiO_2. As the treatment temperature increases, small changes are observed on the surface area and pore volume, which indicates that the treatment temperature exerts a small influence on the textural properties of the catalysts.

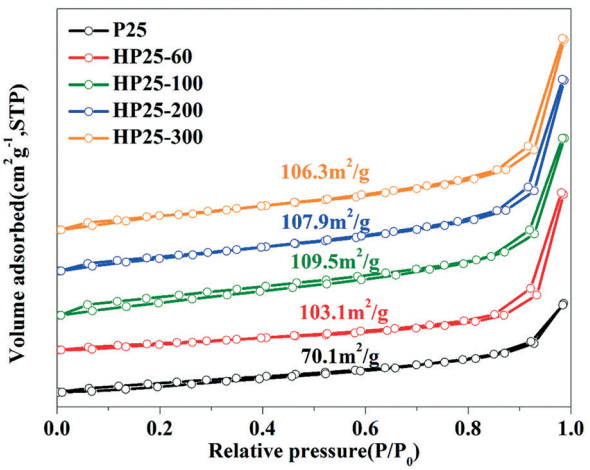

Fig. 7 Nitrogen adsorption–desorption isotherm plots of P25 and HP25-*x* (*x* = 60, 100, 200 and 300).

Table 1 The summary of nitrogen adsorption–desorption isotherm relevant parameters of P25 and HP25-*x* (*x* = 60, 100, 200 and 300)

Catalysis	Surface area (m^2 g^{-1})	Pore volume	Pore diameter
P25	70.1	0.236	3.418
HP25-60	103.1	0.423	3.449
HP25-100	109.5	0.462	3.428
HP25-200	107.9	0.499	3.452
HP25-300	106.3	0.518	3.443

3.3 Optical properties

UV-vis DRS provides information about the optical properties of the prepared samples (Fig. 8a). HP25-*x* and P25 show similar light absorbance in the range of 200–400 nm. Specifically, in comparison to untreated P25, acid treated HP25-*x* samples show a slight red shift in the light absorption range, likely due to the formation of an impurity level between the CB and VB caused by the presence of Ti^{3+} (Fig. 4).[30]

The optical band gap of HP25-*x* and P25 was calculated by using $(\alpha h\nu)^n = A(h\nu - \mathrm{Eg})$ (Fig. 8b), where α is the absorption coefficient, A is the parameter that is related to the effective masses associated with the valence and conduction bands, n is 1/2 for a direct transition, $h\nu$ is the absorption energy, and Eg is the band gap energy, respectively.[31] The band gaps for P25 and HP25-*x* (*x* = 60, 100, 200 and 300) were determined to be 3.15, 3.10, 3.07, 3.11 and 3.11 eV, respectively. This indicates that the band gap changes caused by acid treatment are kind of small.

3.4 Photoelectrochemical analysis

Photocurrent measurement is a technique used to examine the separation rate and transfer efficiency of photo-introduced carriers in a catalytic process[32] (Fig. 9a). In general, the higher photocurrent intensity suggests a higher carrier separation efficiency. The photocurrent sharply increased under light illumination, and simultaneously decayed as the light turned off. This suggests that electrons are excited on the sample surface and transferred to the electrode to generate photo-induced current under light irradiation. HP25-60 shows a much higher photocurrent intensity than the other samples, indicating a much higher carrier separation and transfer efficiency introduced by acid treatment. This is likely because more electrons can be captured by the oxygen vacancies in HP25-60, and more holes can be captured by the Ti^{3+} sites.[19,33] As the treatment temperature increases from 100 to 300 °C, the photocurrent density response decreases substantially likely because the Ti^{3+} sites were re-oxidized into Ti^{4+} sites at higher temperature (Fig. 4).

EIS is also an effective method for probing the charge transfer efficiency at the interface of modified electrodes.[3] EIS plots of P25 and HP25-*x* (*x* = 60, 100, 200 and 300) are displayed in Fig. 9b. The arc radius in the Nyquist plot of HP25-60 is the smallest, indicating that HP25-60 has the

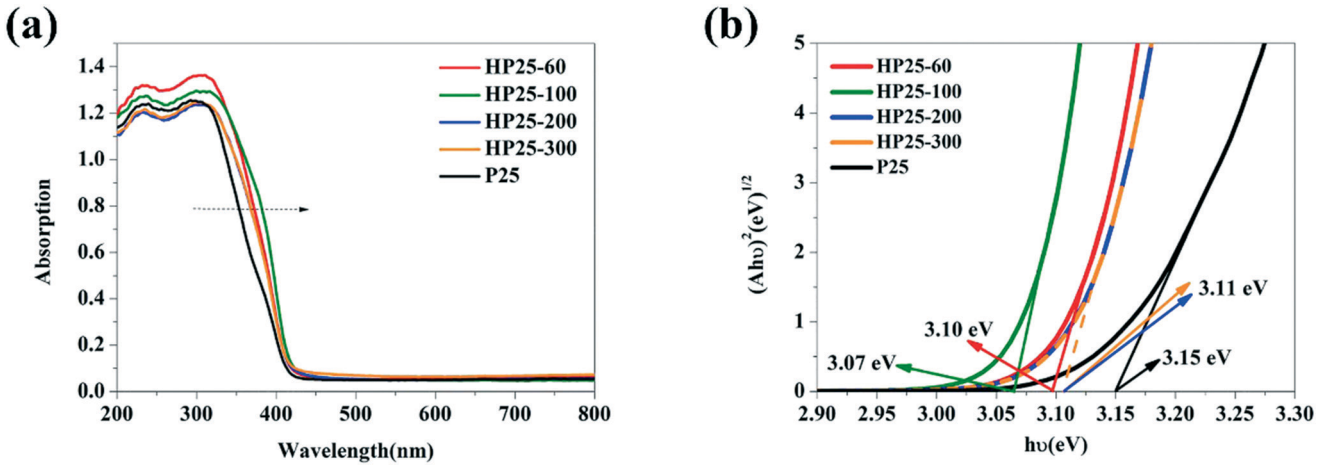

Fig. 8 (a) UV-vis spectra and (b) band gap energy of P25 and HP25-*x* (*x* = 60, 100, 200 and 300).

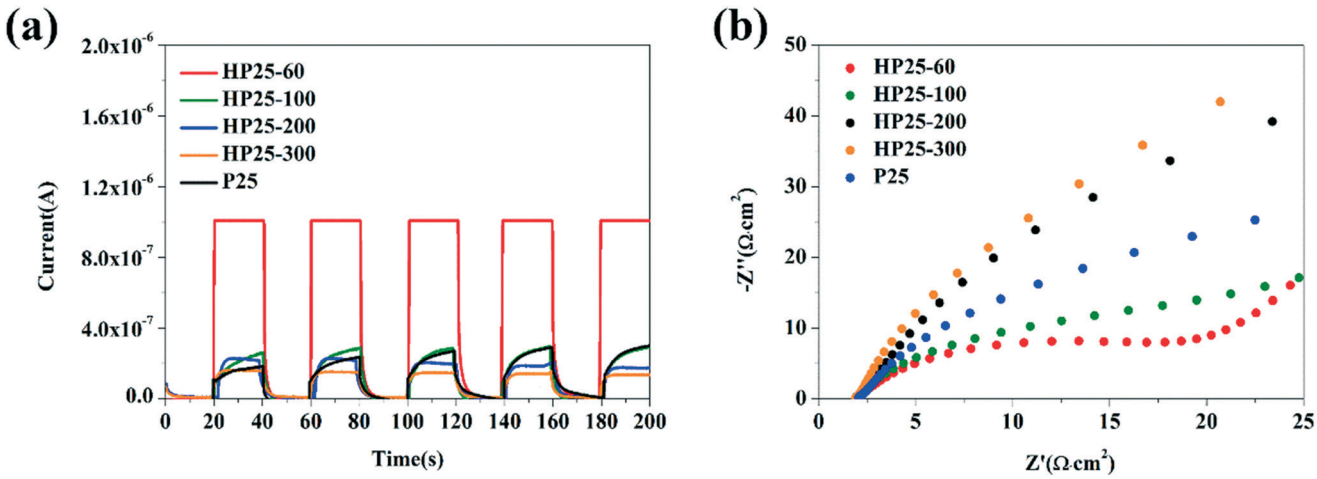

Fig. 9 (a) *J*–*V* curves plotting the photocurrent density as a function of the applied potential. (b) EIS spectra of P25 and HP25-*x* (*x* = 60, 100, 200 and 300) in 0.5 M NaOH ethanol solution.

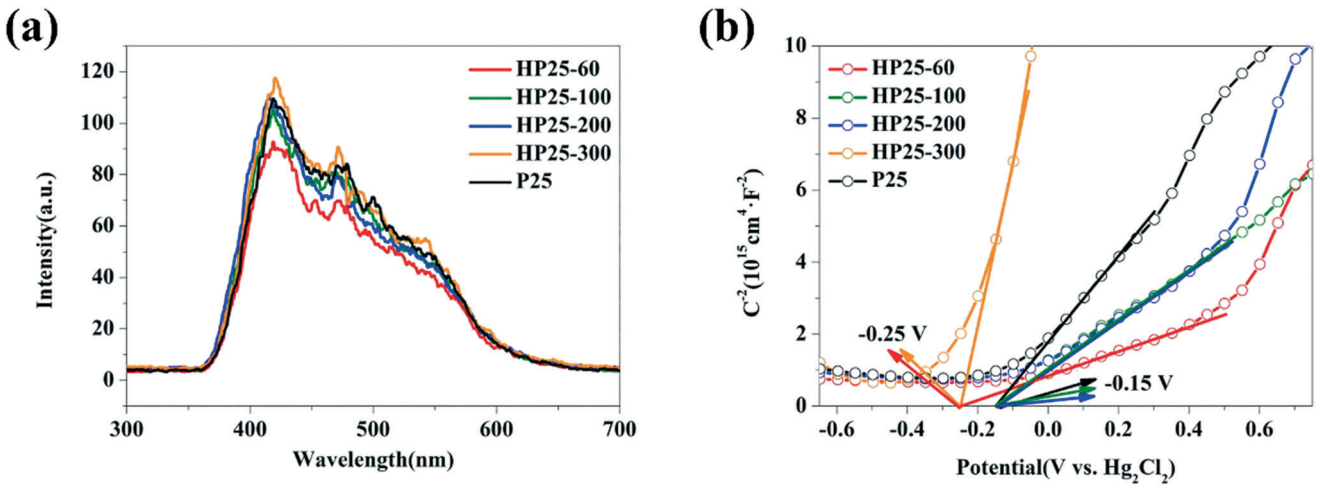

Fig. 10 (a) PL spectra and (b) Mott–Schottky curves of P25 and HP25-*x* (*x* = 60, 100, 200 and 300).

Table 2 The donor density of P25 and HP25-x (x = 60, 100, 200 and 300)

Catalysis	The donor density
P25	1.22×10^{16}
HP25-60	2.35×10^{17}
HP25-100	1.19×10^{17}
HP25-200	1.09×10^{17}
HP25-300	6.07×10^{15}

slowest charge recombination and fastest charge separation, which is consistent with the conclusions obtained from the photocurrent (Fig. 9a).

Photoluminescence (PL) spectroscopy is also an effective technique to study the electronic structure, optical and photochemical properties of semiconductor materials, by which the efficiency of carrier separation can be obtained.[34] The higher the emission peak intensity in the PL spectra, the higher the carrier recombination efficiency. The main emission peaks of HP25-x and P25 appear in the range of 400–600 nm (Fig. 10a). The lowest peak intensity of HP25-60 (Fig. 10a) suggests that HP25-60 possesses the lowest carrier recombination, *i*.e. the highest carrier separation efficiently among all the samples, which is consistent with the conclusions obtained from the photocurrent and impedance characterization.

To better understand the band structure and charge separation of HP25-x and P25, Mott–Schottky analysis was applied (Fig. 10b) and the donor density was calculated using the Mott–Schottky relation [eqn (2)]:

$$\frac{1}{C_{sc}{}^2} = \frac{2}{e\varepsilon\varepsilon_0 N}\left(E_{\text{appl}} - E_{\text{fb}}\right) - \frac{KT}{e} \quad (2)$$

where C_{sc} is the capacitance of the space-charge layer, e is the charge of the electron, ε is the dielectric constant of the semiconductor, ε_0 is the vacuum permittivity of free space, N is the donor density (electron donor concentration for an n-type semiconductor or hole acceptor concentration for a p-type semiconductor), E_{appl} is the applied potential, E_{fb} is the flat-band potential, K is the Boltzmann constant, and T is the absolute temperature.[35] It is generally believed that E_{fb} is 0.1 V below the conduction band position (E_{CB}) for n-type semiconductors.[36] The flat-band potentials (E_{fb}) were calculated and are summarized in Table S1.† The donor density of HP25-60 is 6.8 times higher than that of P25 (Table 2) and is the highest among all the samples which is in good agreement with the photocurrent and EIS results.

3.5 Photocatalytic performance

The H_2 evolution capability over P25 and HP25-x was tested with (Fig. 11) or without (Fig. S1†) Pt as a co-catalyst. After 5 h of reaction, the H_2 production over HP25-60 reached 4852.9 or 1229.2 μmol h^{-1} with or without a Pt co-catalyst, which is 7.1 or 5.3 times higher than 232.3 μmol h^{-1} of P25. The AQY values over HP25-60 with or without a Pt co-catalyst are 21.3% or 5.4%, respectively. However, as the treatment temperature increases from 60 °C to 100, 200 and 300 °C, the hydrogen production decreases significantly, with HP25-200 even producing a lower amount of H_2 than untreated P25. The decrease of hydrogen production at higher acid-treatment temperature can be attributed to the simultaneous decrease of –OH, Ti^{3+} and oxygen vacancies at higher treatment temperature (Fig. 4). On the one hand, the decrease of –OH groups results in a lower amount of Brønsted acid sites, and hence fewer protons for H_2 evolution. On the other hand, the decrease of Ti^{3+} and oxygen vacancies could result in a lower efficiency of carrier separation and transfer, leading to lower hydrogen production.

3.6 Possible photocatalytic mechanism

Based on the above results, a possible mechanism for the enhanced photocatalytic H_2 production efficiency of HP25-x is proposed (Fig. 12). Among all investigated catalysts, HP25-60 has the optimal activity in H_2 photogeneration. After acid treatment,

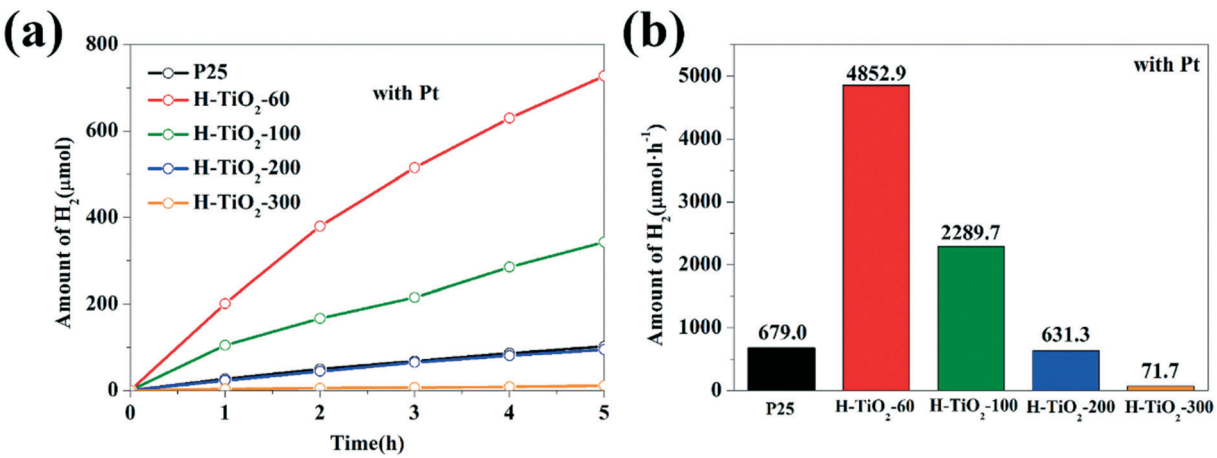

Fig. 11 (a and b) Photocatalytic capacity for H_2 production from water splitting over P25 and HP25-x (x = 60, 100, 200 and 300) under the conditions with Pt as a co-catalyst.

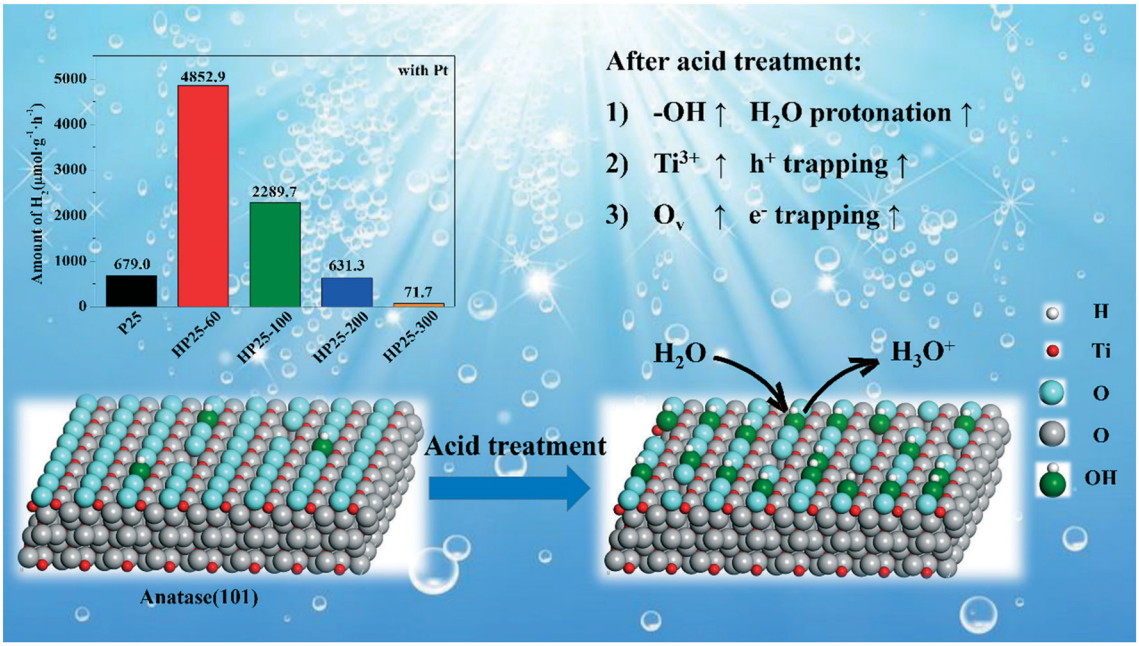

Fig. 12 Possible photocatalytic mechanism of photocatalytic H_2 production over HP25-60 under simulated light.

the contents of –OH, Ti^{3+} and oxygen vacancies increase significantly (Fig. 4). On the one hand, the substantial amount of –OH groups introduced by acid treatment could act as Brønsted acid sites enhancing the water adsorption and providing protons for H_2 evolution.[14] On the other hand, after acid treatment, more electrons can be captured by more oxygen vacancies in HP25-60, and more holes can be captured by more Ti^{3+} sites, resulting in an enhanced carrier separation and transfer efficiency. Although the red shift of the light absorption scope can be observed, such a slight shift introduced by acid treatment exerts a faint influence on the band gap and the light absorption capability of P25, which suggests that this effect can be removed from the reasons for enhanced H_2 production. To sum up, the enhanced photocatalytic H_2 production activity of HP25-60 is mainly attributed to the co-effect of Brønsted acid sites, Ti^{3+} and oxygen vacancies. Such a modification strategy can be used as a universally applicable method for other valence-alternative metal oxide semiconductors for H_2 photogeneration.

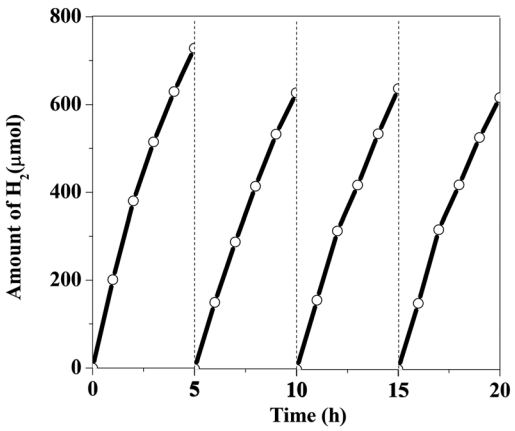

Fig. 13 Repeated photocatalytic hydrogen production experiments over HP25-60.

3.7 Stability evaluation

Photocatalyst recycle experiments of HP25-60 were carried out to examine the catalyst stability (Fig. 13). The recycled HP25-60 still shows a high photocatalytic H_2 production rate after 4 cycles, indicating that the acid treated P25 possesses excellent stability during H_2 evolution experiments.

4. Conclusions

In this paper, highly efficient P25 catalysts for photocatalytic H_2 evolution were successfully fabricated *via* a simple acid treatment (HP25-*x*, *x* = 60, 100, 200 and 300). After 5 h of reaction, the H_2 production over HP25-60 reached 4852.9 or 1229.2 μmol h^{-1} with or without a Pt co-catalyst, respectively, which is 7.1 or 5.3 times higher than 232.3 μmol h^{-1} of P25. The enhanced photocatalytic H_2 production activity of HP25-60 is due to the presence of substantial Brønsted acid sites, as well as Ti^{3+} sites and oxygen vacancies. The Brønsted acid sites can protonate H_2O, hence enhancing H_2O adsorption and providing protons for H_2 production. The Ti^{3+} sites and oxygen vacancies can suppress carrier recombination and promote carrier transfer efficiency by trapping electrons and holes, respectively. Such a simple acid treatment strategy can be used as a universally applicable method for modification of other photocatalysts (*e.g.* valence-alternative metal oxide semiconductors) for enhanced H_2 photogeneration.

Conflicts of interest

There are no conflicts to declare.

Acknowledgements

This work was supported by the Youth Foundation of Qingdao Application and Basic Research (No. 19-6-2-16-cg), Doctoral Fund of Qingdao Agricultural University (No. 663/1118005) and National Natural Science Foundation of China (No. 11804180).

References

1 J. Yu, Y. Hai and B. Cheng, Enhanced Photocatalytic H2-Production Activity of TiO_2 by $Ni(OH)_2$ Cluster Modification, *J. Phys. Chem. C*, 2011, **115**, 4953–4958.

2 S. Xu and D. D. Sun, Significant improvement of photocatalytic hydrogen generation rate over TiO_2 with deposited CuO, *Int. J. Hydrogen Energy*, 2009, **34**, 6096–6104.

3 Y. Wang, J. Cai, M. Wu, H. Zhang, M. Meng, Y. Tian, T. Ding, J. Gong, Z. Jiang and X. Li, Hydrogenated Cagelike Titania Hollow Spherical Photocatalysts for Hydrogen Evolution under Simulated Solar Light Irradiation, *ACS Appl. Mater. Interfaces*, 2016, **8**, 23006–23014.

4 K. Maeda and K. Domen, Photocatalytic Water Splitting: Recent Progress and Future Challenges, *J. Phys. Chem. Lett.*, 2010, **1**, 2655–2661.

5 T. Ouyang, Y.-Q. Ye, C.-Y. Wu, K. Xiao and Z.-Q. Liu, Heterostructures Composed of N-Doped Carbon Nanotubes Encapsulating Cobalt and β-Mo_2C Nanoparticles as Bifunctional Electrodes for Water Splitting, *Angew. Chem., Int. Ed.*, 2019, **58**, 4923–4928.

6 M. Xing, B. Chen, J. Feng, W. Xu, Y. Bai, Y. Zhou, C. Dong, H. Zhong, J. Zhang and Y. Yin, Confined Growth of Quantum Dots in Silica Spheres by Ion Exchange of "Trapped NH_4^+" for White-Light Emission, *Chem*, 2019, **5**, 2195–2214.

7 Q. Zhu, B. Qiu, H. Duan, Y. Gong, Z. Qin, B. Shen, M. Xing and J. Zhang, Electron directed migration cooperated with thermodynamic regulation over bimetallic NiFeP/g-C_3N_4 for enhanced photocatalytic hydrogen evolution, *Appl. Catal., B*, 2019, **259**, 118078.

8 Z. Zou, J. Ye, K. Sayama and H. Arakawa, Direct splitting of water under visible light irradiation with an oxide semiconductor photocatalyst, *Nature*, 2001, **414**, 625–627.

9 Z. Jin, X. Zhang, Y. Li, S. Li and G. Lu, 5.1% Apparent quantum efficiency for stable hydrogen generation over eosin-sensitized CuO/TiO_2 photocatalyst under visible light irradiation, *Catal. Commun.*, 2007, **8**, 1267–1273.

10 J. Hämäläinen, M. Ritala and M. Leskelä, Atomic Layer Deposition of Noble Metals and Their Oxides, *Chem. Mater.*, 2014, **26**, 786–801.

11 L. Yang, J. Liu, L. Yang, M. Zhang, H. Zhu, F. Wang and J. Yin, Co3O4 imbedded g-C_3N_4 heterojunction photocatalysts for visible-light-driven hydrogen evolution, *Renewable Energy*, 2020, **145**, 691–698.

12 R. Abe, K. Sayama and H. Arakawa, Dye-sensitized photocatalysts for efficient hydrogen production from aqueous I− solution under visible light irradiation, *J. Photochem. Photobiol., A*, 2004, **166**, 115–122.

13 M. Du, B. Qiu, Q. Zhu, M. Xing and J. Zhang, Fluorine doped TiO_2/mesocellular foams with an efficient photocatalytic activity, *Catal. Today*, 2019, **327**, 340–346.

14 S. K. Park and H. Shin, Effect of HCl and H_2SO_4 treatment of TiO_2 powder on the photosensitized degradation of aqueous rhodamine B under visible light, *J. Nanosci. Nanotechnol.*, 2014, **14**, 8122–8128.

15 S. Hao, J. Wu, L. Fan, Y. Huang, J. Lin and Y. Wei, The influence of acid treatment of TiO_2 porous film electrode on photoelectric performance of dye-sensitized solar cell, *Sol. Energy*, 2004, **76**, 745–750.

16 K.-H. Park, E. M. Jin, H. B. Gu, S. E. Shim and C. K. Hong, Effects of HNO_3 treatment of TiO_2 nanoparticles on the photovoltaic properties of dye-sensitized solar cells, *Mater. Lett.*, 2009, **63**, 2208–2211.

17 C. Lv, X. Lan, L. Wang, X. Dai, M. Zhang, J. Cui, S. Yuan, S. Wang and J. Shi, Rapidly and highly efficient degradation of tetracycline hydrochloride in wastewater by 3D IO-TiO_2-CdS nanocomposite under visible light, *Environ. Technol.*, 2019, 1–11.

18 S. Yurdakal, G. Palmisano, V. Loddo, V. Augugliaro and L. Palmisano, Nanostructured Rutile TiO_2 for Selective Photocatalytic Oxidation of Aromatic Alcohols to Aldehydes in Water, *J. Am. Chem. Soc.*, 2008, **130**, 1568–1569.

19 J. Kuang, Z. Xing, J. Yin, Z. Li, S. Tan, M. Li, J. Jiang, Q. Zhu and W. Zhou, Ti^{3+} self-doped rutile/anatase/TiO_2(B) mixed-crystal tri-phase heterojunctions as effective visible-light-driven photocatalysts, *Arabian J. Chem.*, 2018, DOI: 10.1016/j.arabjc.2018.06.010.

20 Z.-S. Wang, K. Hara, Y. Dan-oh, C. Kasada, A. Shinpo, S. Suga, H. Arakawa and H. Sugihara, Photophysical and (Photo)electrochemical Properties of a Coumarin Dye, *J. Phys. Chem. B*, 2005, **109**, 3907–3914.

21 H. S. Jung, J.-K. Lee, S. Lee, K. S. Hong and H. Shin, Acid Adsorption on TiO_2 Nanoparticles—An Electrochemical Properties Study, *J. Phys. Chem. C*, 2008, **112**, 8476–8480.

22 L. Wang, Y. Yu, H. He, Y. Zhang, X. Qin and B. Wang, Oxygen vacancy clusters essential for the catalytic activity of CeO_2 nanocubes for *o*-xylene oxidation, *Sci. Rep.*, 2017, **7**, 12845.

23 S. Chen, H. Wang, Z. Kang, S. Jin, X. Zhang, X. Zheng, Z. Qi, J. Zhu, B. Pan and Y. Xie, Oxygen vacancy associated single-electron transfer for photofixation of CO_2 to long-chain chemicals, *Nat. Commun.*, 2019, **10**, 788.

24 X. Pan, M.-Q. Yang, X. Fu, N. Zhang and Y.-J. Xu, Defective TiO_2 with oxygen vacancies: synthesis, properties and photocatalytic applications, *Nanoscale*, 2013, **5**, 3601–3614.

25 I. Nakamura, N. Negishi, S. Kutsuna, T. Ihara, S. Sugihara and K. Takeuchi, Role of oxygen vacancy in the plasma-treated TiO_2 photocatalyst with visible light activity for NO removal, *J. Mol. Catal. A: Chem.*, 2000, **161**, 205–212.

26 D. Zhao, C. Chen, Y. Wang, H. Ji, W. Ma, L. Zang and J. Zhao, Surface Modification of TiO_2 by Phosphate: Effect on Photocatalytic Activity and Mechanism Implication, *J. Phys. Chem. C*, 2008, **112**, 5993–6001.

27 J. Zhu, J. Yang, Z.-F. Bian, J. Ren, Y.-M. Liu, Y. Cao, H.-X. Li, H.-Y. He and K.-N. Fan, Nanocrystalline anatase TiO_2 photocatalysts prepared via a facile low temperature nonhydrolytic sol–gel reaction of $TiCl_4$ and benzyl alcohol, *Appl. Catal., B*, 2007, **76**, 82–91.

28 K. Nagaveni, M. S. Hegde, N. Ravishankar, G. N. Subbanna and G. Madras, Synthesis and Structure of Nanocrystalline TiO_2 with Lower Band Gap Showing High Photocatalytic Activity, *Langmuir*, 2004, **20**, 2900–2907.

29 A. Ketabchi, K. Komm, M. Miles-Rossouw, D. A. D. Cassani and F. Variola, Nanoporous Titanium Surfaces for Sustained Elution of Proteins and Antibiotics, *PLoS One*, 2014, **9**, e92080.

30 S. Wang, J. Cai, J. Mao, S. Li, J. Shen, S. Gao, J. Huang, X. Wang, I. P. Parkin and Y. Lai, Defective black Ti^{3+} self-doped TiO_2 and reduced graphene oxide composite nanoparticles for boosting visible-light driven photocatalytic and photoelectrochemical activity, *Appl. Surf. Sci.*, 2019, **467-468**, 45–55.

31 M. Yoon, M. Seo, C. Jeong, J. H. Jang and K. S. Jeon, Synthesis of Liposome-Templated Titania Nanodisks: Optical Properties and Photocatalytic Activities, *Chem. Mater.*, 2005, **17**, 6069–6079.

32 H. Cui, Y. Liu, W. Ren, M. Wang and Y. Zhao, Large scale synthesis of highly crystallized SnO_2 quantum dots at room temperature and their high electrochemical performance, *Nanotechnology*, 2013, **24**(34), 345602-5.

33 J. Yin, Z. Xing, J. Kuang, Z. Li, M. Li, J. Jiang, S. Tan, Q. Zhu and W. Zhou, Bi plasmon-enhanced mesoporous Bi_2MoO_6/Ti^{3+} self-doped TiO_2 microsphere heterojunctions as efficient visible-light-driven photocatalysts, *J. Alloys Compd.*, 2018, **750**, 659–668.

34 X. Z. Li and F. B. Li, Study of Au/Au^{3+}-TiO_2 Photocatalysts toward Visible Photooxidation for Water and Wastewater Treatment, *Environ. Sci. Technol.*, 2001, **35**, 2381–2387.

35 H. Huang, Y. He, X. Li, M. Li, C. Zeng, F. Dong, X. Du, T. Zhang and Y. Zhang, $Bi_2O_2(OH)(NO_3)$ as a desirable $[Bi_2O_2]^{2+}$ layered photocatalyst: strong intrinsic polarity, rational band structure and {001} active facets co-beneficial for robust photooxidation capability, *J. Mater. Chem. A*, 2015, **3**, 24547–24556.

36 C. Zeng, Y. Hu and H. Huang, $BiOBr_{0.75}I_{0.25}$/$BiOIO_3$ as a Novel Heterojunctional Photocatalyst with Superior Visible-Light-Driven Photocatalytic Activity in Removing Diverse Industrial Pollutants, *ACS Sustainable Chem. Eng.*, 2017, **5**, 3897–3905.